ChemComm

COMMUNICATION

View Article Online
View Journal | View Issue

Cite this: *Chem. Commun.*, 2022, **58**, 11949

Received 29th July 2022,
Accepted 29th September 2022

DOI: 10.1039/d2cc04241j

rsc.li/chemcomm

Formation of new crystalline qtz-$[Zn(mIm)_2]$ polymorph from amorphous ZIF-8†

Michael F. Thorne, ‡[a] Celia Castillo-Blas, ‡[a] Lauren N. McHugh, [a] Alice M. Bumstead, [a] Georgina Robertson,[a] Adam F. Sapnik, [a] Chloe S. Coates, [b] Farheen N. Sayed, [b] Clare P. Grey, [b] David A. Keen, [c] Martin Etter,[d] Ivan da Silva, [c] Krunoslav Užarević [e] and Thomas D. Bennett *[a]

The structure of a new ZIF-8 polymorph with quartz topology (qtz) is reported. This qtz-$[Zn(mIm)_2]$ phase was obtained by mechanically amorphising crystalline ZIF-8, before heating the resultant amorphous phase to between 282 and 316 °C. The high-temperature phase structure was obtained from powder X-ray diffraction, and its thermal behaviour, CO_2 gas sorption properties and dye adsorption ability were investigated.

Zeolitic imidazolate frameworks (ZIFs) are a subclass of metal–organic frameworks (MOFs) which contain M^{2+} cations, often Zn^{2+}, linked by imidazolate anions.[1,2] ZIFs have been noted for their exceptionally high thermal stability with respect to other MOFs,[3] and have potential applications in gas separation, chemical sensing, drug delivery and catalysis.[4]

The rich energetic landscape of ZIFs leads to interesting polymorphic behaviour and amorphisation.[5] ZIFs are typically prepared as crystalline powders. Amorphous MOFs have gained, however, great attention in recent years. They retain the building blocks and connectivity of their crystalline counterparts,[6] though they lack long-range order. Despite this, they possess very promising optical and mechanical properties for practical applications.[7]

The amorphous phase of ZIFs (aZIFs) can be accessed by melt-quenching,[8] thermal amorphisation of a crystalline ZIF,[9] or, more universally, by mechanical milling.[6] Melting or thermal amorphisation of crystalline ZIFs is, however, somewhat challenging and is therefore not always a widely applicable approach.[10] The low density of many crystalline ZIFs means the temperature required to access the liquid state is far above their decomposition temperatures (T_d). This is due to the high free energy barrier for the decoordination and reattachment of imidazolate linkers from the metal cations during melting.[10,11] On the other hand, mechanical amorphisation is a reliable way to obtain amorphous ZIFs, and is typically achieved within one hour of milling.[12,13] Amorphisation of ZIF-4, $[Zn(Im)_2]$ – where Im = imidazolate $(C_3N_2H_3)^-$, for example, occurs in under 30 minutes. The amorphous product, a_mZIF-4, curiously undergoes crystallisation to the dense ZIF-zni phase upon heating to 475 °C.[14,15]

Mechanical amorphisation has also been reported for a_mZIF-62 $[Zn(Im)_{2-x}(bIm)_x]$ and a_mZIF-UC-5 $[Zn(Im)_{2-x}(ClbIm)_x]$ materials, where bIm = benzimidazolate $(C_7N_2H_5)^-$, and ClbIm = 5-chlorobenzimdazolate $(C_7N_2H_4Cl)^-$.[16] The inclusion of substituted imidazolate linkers, such as bIm and ClbIm, traps the a_mZIFs in a metastable amorphous phase upon heating.[16] The crystallisation of a_mZIF-4 and the glass transition temperature (T_g) of a_mZIF-62 highlight the importance of investigating the thermal response of aZIFs in general, as it may be possible to induce similar transitions in other aZIFs. T_g is the temperature in amorphous materials where the reversible transition between a glassy state and a viscoelastic state occurs.

ZIF-8 $[Zn(mIm)_2]$, mIm = 2-methylimidazolate $(C_4N_2H_5)^-$ with sodalite (**SOD**) topology, is a widely studied, prototypical ZIF.[17–19] ZIF-8 is of great interest due to its high porosity and relatively high thermal stability compared to most MOFs.[3] Further to this, ZIF-8 is one of the few commercially-manufactured ZIFs, being sold under the name Basolite® Z1200.[20]

Mechanical amorphisation of ZIF-8 has been previously reported in a vibratory ball mill, yielding a_mZIF-8.[21] X-ray total scattering experiments and subsequent refinements using Reverse Monte Carlo modelling revealed a_mZIF-8 retains the short-range order of ZIF-8 $[Zn(mIm)_2]$ whilst displaying a continuous random network (CRN) topology.[21] The thermal stability compared to mass loss of a_mZIF-8 was also investigated, using thermogravimetric analysis (TGA).[21] This revealed a

[a] *Department of Materials Science and Metallurgy, University of Cambridge, 27 Charles Babbage Road, Cambridge, CB3 0FS, UK. E-mail: tdb35@cam.ac.uk*
[b] *Yusuf Hamied Department of Chemistry, University of Cambridge, Lensfield Road, Cambridge, CB2 1EW, UK*
[c] *ISIS Facility, STFC Rutherford Appleton Laboratory, Chilton, Didcot, OX11 0QX, UK*
[d] *Deutsches Elektronen Synchrotron, FS-PETRA-D, P02.1, Notkestr. 85, 22607, Hamburg, Germany*
[e] *Ruđer Bošković Institute, Bijenička Cesta 54, Zagreb, HR-10000, Croatia*

† Electronic supplementary information (ESI) available. CCDC 2149756. For ESI and crystallographic data in CIF or other electronic format see DOI: https://doi.org/10.1039/d2cc04241j

‡ These authors contributed equally to this work.

decrease in thermal stability at elevated temperatures with respect to crystalline ZIF-8. No other thermal measurements were performed.

Furthermore, ZIF-8 is able to transform into other crystalline polymorphs by mechanical milling. For example, milling for 35 minutes results in sequential crystallisation of a_mZIF-8 to the relatively dense [Zn(mIm)$_2$] polymorphs **kat-[Zn(mIm)$_2$]** and **dia-[Zn(mIm)$_2$]**, where **kat** and **dia** refer to the topologies of the new crystalline phases.[22] This extended milling time of a_mZIF-8 is analogous to heating a_mZIF-4,[14] where energy is supplied to the metastable amorphous phase, allowing crystallisation to ZIF-**zni** to occur. This suggests that the additional energy supplied by milling facilitates linker mobility, and therefore potential phase transitions.

While the thermal stability of MOFs is generally determined by TGA, this technique provides no information on potential phase changes that may occur during heating. Therefore, other techniques such as DSC should be performed to identify potential new phases.[23]

Here we investigate whether any additional phases are formed upon heating a_mZIF-8, using DSC and TGA. First, crystalline ZIF-8 was synthesised following the reported methodology.[19] Powder X-ray diffraction (PXRD) was performed on the resulting white solid in order to confirm the phase purity through a Pawley refinement (Fig. S1 and Table S1, ESI†).[24] ZIF-8 was then mechanochemically amorphised in a vibratory ball mill (see Methods). *In situ* monitoring of the process by synchrotron PXRD confirmed direct amorphisation of ZIF-8 was completed after 40 minutes of ball milling to yield a_mZIF-8. The lack of unassigned Bragg peaks also confirms that the amorphisation process occurred without the formation of any new phases (Fig. 1a and Fig. S2, ESI†). Whilst heating to 1000 °C, a_mZIF-8 showed major decomposition above 400 °C (Fig. S3, ESI†). Guided by this, DSC analysis of a_mZIF-8 under an argon atmosphere was only performed up to 400 °C, where a single exothermic transition was observed (Fig. 1b). The onset of this event occurred at 282.0 °C, *i.e.* before significant mass loss occurred and it corresponds to an enthalpy change of -22.3 J g^{-1} (-5.31 kJ mol^{-1}) (Fig. 1b and Fig. S4, ESI†). After heating the sample to 400 °C and subsequently cooling to room temperature, PXRD confirmed the formation of a crystalline phase (Fig. 1c and Fig. S4, ESI†). Therefore, the exothermic transition may be denoted as T_x (= 282 °C), where ΔH_x = -5.31 kJ mol^{-1} and ΔS_x = -9.14 J mol^{-1} K^{-1} (Fig. 1b). The T_x at elevated temperatures highlights the metastability of amorphous ZIFs compared to their crystalline counterparts, as a significant amount of energy is released from a_mZIF-8 upon crystallisation. Surprisingly, using the same DSC experimental conditions, this phase transition was not detected under a nitrogen atmosphere.

The ball-milling amorphisation step in the synthesis of this new phase meant that the particle size of the crystallised sample was small (<5 μm) and was hence not suitable for single crystal X-ray diffraction (Fig. S5 and S6, ESI†). Therefore, to produce an atomic-scale model of this new phase, structural solution from PXRD data was performed. A high-resolution

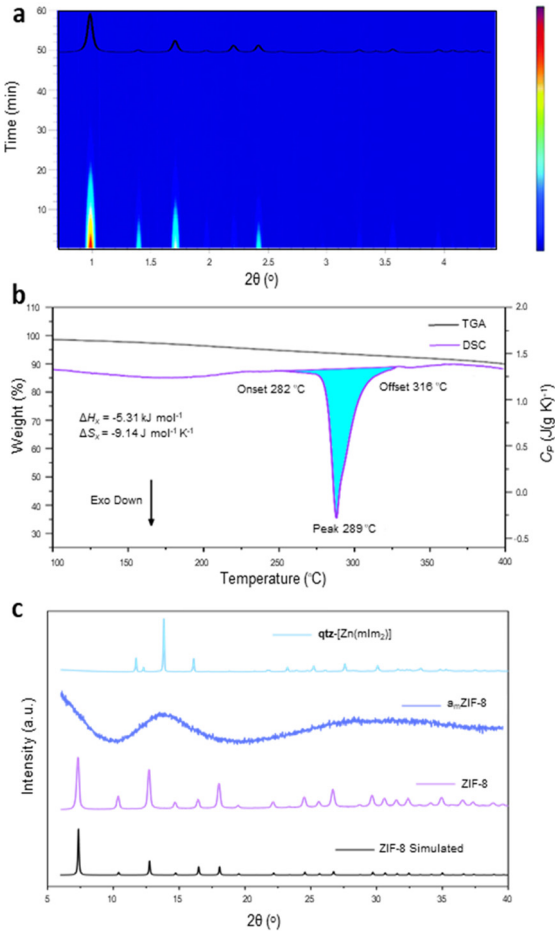

Fig. 1 (a) *In situ* PXRD ball milling amorphisation of ZIF-8 showing complete amorphisation after 40 minutes of milling (λ = 0.20735 Å). Red = high intensity, blue = low intensity. Inset: Calculated ZIF-8 PXRD pattern from a literature CIF.[20] (b) DSC-TGA scan of a_mZIF-8 exhibiting a T_x onset = 282 °C. (c) PXRD patterns (Cu-source) of the simulated ZIF-8,[20] experimental a_mZIF-8 and the new phase obtained after heating a_mZIF-8 to 400 °C.

diffraction pattern was collected on the I11 beamline (Diamond Light Source synchrotron) using X-rays with a wavelength of λ = 0.82697 Å. The pattern was indexed using Materials Studio Suite, with a hexagonal unit cell and with parameters a = 17.3621(8) Å, c = 24.0711(9) Å, V = 6283.926(17) Å^3, in the space group $P6_122$. A Pawley refinement based on this cell and space group was performed to obtain integrated intensities (F_{obs}^2) (Table S2 and Fig. S7, ESI†). Electron density maps were produced using the charge flipping method (Fig. 2a and Fig. S8, ESI†).[25] Zn positions were identified from the map at special positions with a total of 24 Zn atoms per unit cell (Fig. 2b and Fig. S8, ESI†). C and N atomic positions were refined constraining the mIm linker as a rigid body. The structural model was refined against the diffraction pattern using the Rietveld method (Tables S3 and S9, ESI†). The resulting topology was identified as **qtz** (Fig. 2c and Fig. S10, ESI†), using TOPOS pro.

According to ^{1}H-NMR and CHN microanalyses, **qtz-[Zn(mIm)$_2$]** retains the mIm linker and no new proton

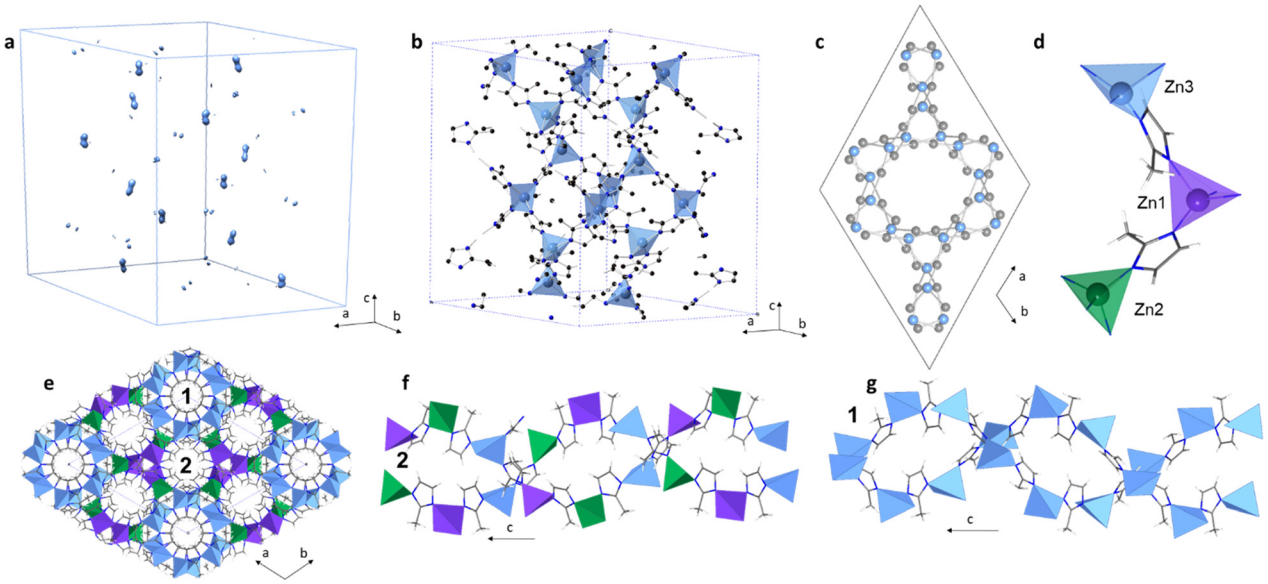

Fig. 2 (a) 3D Electron density map. Zn atoms are still visible whilst light atoms (C and N) are difficult to assign; (b) final refined structural model including mIm linkers in the structure as rigid bodies. Zn (tetrahedral cyan), N (blue), carbon (black). (c) Simplified net of the **qtz-[Zn(mIm)$_2$]**. Zn (blue), mIm (grey); (d) different coordination environments of the three crystallographically independent Zn atoms; (e) view of the final refined model along the *c* axis. Zn1 (purple), Zn2 (green) and Zn3 (cyan), N (blue), carbon (grey). Hydrogens were omitted for clarity; (f) and (g) double helixes formed along the *a* axis.

environments form during its crystallisation (Fig. S11 and Table S4, ESI†). Furthermore, **qtz-[Zn(mIm)$_2$]** exhibited an almost identical Fourier transform infrared spectrum to both ZIF-8 and a$_m$ZIF-8, thus indicating the retention of local chemical bonding across all three phases (Fig. S12, ESI†). TGA revealed **qtz-[Zn(mIm)$_2$]** was thermally stable under argon up to 452 °C, above which it began to decompose rapidly (Fig. S13, ESI†). Multiple heating cycles to 450 °C were performed on **qtz-[Zn(mIm)$_2$]**, though DSC indicated no further phase transitions, suggesting that this crystalline polymorph is thermodynamically stable (Fig. S14, ESI†). This is in agreement with previous studies which identify the **qtz** topology as one of the most thermodynamically stable crystalline ZIF topologies.[26] Surprisingly, the **qtz**-ZIF-8 material has only been achieved in the presence of the eIm linker, where eIm = 2-ethyl imidazolate $(C_5H_7N_2)^-$.[27] In an incredibly recent study, a material exhibiting the **qtz** topology was prepared by heating a sample of nanosized (20 nm) crystalline **SOD-[Zn(mIm)$_2$]**.[28] However, in this case, the authors were not able to obtain cell parameters, or atomic positions within this previously unknown structure. The **qtz-[Zn(mIm)$_2$]** has some differences to other previously published **qtz** topology ZIFs, **qtz-[M(eIm)$_2$]** where M = Zn,29 Fe and Co,[27] and [Fe(mIm)$_2$].[30] Both **qtz-[Fe(mIm)$_2$]** and **qtz-[M(eIm)$_2$]** possess one unique M equivalent position, whilst **qtz-[Zn(mIm)$_2$]** has three distinct Zn atomic positions each with a distorted tetrahedral environment (Fig. 2d and Fig. S15, Table S5, ESI†). All **qtz** structures show double helices and channels along the *c* axis (Fig. S16 and 17, ESI†). **qtz-[Zn(mIm)$_2$]** has two different channels, where the first one is located along (0, 0, *z*), and the second one is along (1/2, 1/2, *z*) and equivalents (Fig. 2e–g). To further confirm that the structure is a new **qtz-[Zn(mIm)$_2$]** polymorph, a comparison of our experimental PXRD data to the dense **dia-[Zn(mIm)$_2$]** polymorph is presented in Fig. S18 (ESI†). This clearly highlights the different positions of the Bragg reflections exhibited by the **dia** and **qtz** [Zn(mIm)$_2$] structures.

Gas sorption experiments were performed on ZIF-8, a$_m$ZIF-8, and **qtz-[Zn(mIm)$_2$]**, to investigate their porosity (Fig. S19, ESI†). These showed that **qtz-[Zn(mIm)$_2$]** has a lower total CO_2 uptake than ZIF-8 and a$_m$ZIF-8; maximum volumes of CO_2 adsorbed for ZIF-8, a$_m$ZIF-8 and **qtz-[Zn(mIm)$_2$]** were 37.6, 18.6 and 6.5 cm^3 g^{-1} STP, respectively. This is likely because **qtz-[Zn(mIm)$_2$]** is a denser phase than a$_m$ZIF-8 and ZIF-8. At higher gas pressures, a$_m$[Zn(mIm)$_2$], and especially **qtz-[Zn(mIm)$_2$]**, showed signs of CO_2 uptake plateauing, while ZIF-8 remained unsaturated even at the maximum pressure used during these measurements. a$_m$ZIF-8 shows the largest adsorption–desorption hysteresis due to a kinetic effect caused by the lack of regular pore structure, which restricts CO_2 desorption from the material.

To further investigate porosity differences between the three polymorphs of ZIF-8, absorption of methylene blue (MB) dye from an aqueous solution was investigated. MB was chosen as it has been shown to be adsorbed by ZIF-8, where the adsorption mechanism was studied.[31] After 48 hours of stirring powdered ZIF samples in a 5 ppm aqueous solution, followed by filtration (see Methods), it was clear on visual inspection that the adsorption of MB by the various ZIF-8 polymorphs followed the trend in porosity seen from CO_2 gas absorption experiments, though MB molecules may also be situated in the space between particles (Fig. S20, ESI†). Dye uptake values were determined from UV-VIS absorbance spectra of the remaining solutions at 665 nm by comparing to a calibration curve (Fig. S20, ESI†). The observed trend for MB adsorption was ZIF-8 > a$_m$ZIF-8 > **qtz-[Zn(mIm)$_2$]**, with absorbance percentages

of 92.8%, 80.0% and 43.1% respectively (Fig. S22 and Table. S6, ESI†). This trend might be related with the larger particle size of the **qtz-[Zn(mIm)$_2$]** phase compared to the small particle size of a_mZIF-8. These results highlight two important points. Firstly, that a_mZIFs still possess desirable properties, and even exhibit higher uptake of gases and organic molecules than some crystalline polymorphs, *i.e.*, a_mZIF-8 > **qtz-[Zn(mIm)$_2$]**. Secondly, these results show how total gas uptake and crystallinity are not always good predictors of a material's performance in other applications, as **qtz-[Zn(mIm)$_2$]**, and especially a_mZIF-8, possess far higher dye adsorption than might be first anticipated from their gas uptake properties (Fig. S22, ESI†).

In conclusion, we demonstrate the formation of a new crystalline polymorph of ZIF-8, **qtz-[Zn(mIm)$_2$]**, from mechanically amorphised ZIF-8. This was achieved by heating a_mZIF-8 under an argon atmosphere. **qtz-[Zn(mIm)$_2$]** has lower CO_2 uptake than a_mZIF-8 or ZIF-8; most likely due to the high structural density of **qtz-[Zn(mIm)$_2$]** and its narrow pores. The formation of new crystalline polymorphs obtained by heating the amorphous phases illustrates the complex energetic landscape of ZIF materials and highlights the importance of the amorphous phases of MOFs as metastable intermediates in the formation of new crystalline polymorphs. This study opens up new possibilities for obtaining unprecedented ZIF topologies, even in highly investigated systems such as ZIF-8, by combining mechanochemistry with other energy sources. It also provides firm evidence of the possible utility of a_mZIFs in water remediation applications.

M. F. T. thanks Corning Incorporated for PhD funding. C. C. B., L. N. M. and T. D. B. acknowledge the Leverhulme Trust for a Research Project Grant (RPG-2020-005), and a Philip Leverhulme Prize (2019). T. D. B., A. M. B. thank the Royal Society (UF150021, RFG\EA\180092, RSG\R1\180395 and RGS\R2\212221). A. F. S. acknowledges the EPSRC under industrial CASE scheme along with Johnson Matthey PLC (JM11106). K. U. thanks the Croatian Science Foundation and the European Social Fund for financial support (PZS-2019-02-4129). We extend our gratitude to Diamond Light Source (United Kingdom), and DESY (Germany) for access to beamlines I11(CY28349-5) and P02.1, respectively.

M. F. T. and C. C. B. conceptualised the project and wrote the manuscript with input of all authors. M. F. T. synthesised and characterised the materials and carried out UV-VIS experiments. L. N. M. collected CO_2 isotherms. G. R. collected SEM images. A. M. B., A. F. S. and D. A. K. contributed with useful discussions. C. S. C., F. H. and C. G. collected the PXRD pattern at I-11. M. E., M. F. T. and K. U. collected *in situ* ball milling XRD experiments. C. C. B. and I. d. S. solved and refined the **qtz-[Zn(mIm)$_2$]** structure. T. D. B. supervised the project and acquired funding.

Conflicts of interest

There are no conflicts to declare.

References

1 K. S. Park, Z. Ni, A. P. Côté, J. Y. Choi, R. Huang, F. J. Uribe-Romo, H. K. Chae, M. O'Keeffe and O. M. Yaghi, *Proc. Natl. Acad. Sci. U. S. A.*, 2006, **103**, 10186–10191.
2 Y.-Q. Tian, C.-X. Cai, Y. Ji, X.-Z. You, S.-M. Peng and G.-H. Lee, *Angew. Chem., Int. Ed.*, 2002, **41**, 1384–1386.
3 C. Healy, K. M. Patil, B. H. Wilson, L. Hermanspahn, N. C. Harvey-Reid, B. I. Howard, C. Kleinjan, J. Kolien, F. Payet, S. G. Telfer, P. E. Kruger and T. D. Bennett, *Coord. Chem. Rev.*, 2020, **419**, 213388.
4 B. Chen, Z. Yang, Y. Zhu and Y. Xia, *J. Mater. Chem. A*, 2014, **2**, 16811–16831.
5 R. N. Widmer, G. I. Lampronti, S. Chibani, C. W. Wilson, S. Anzellini, S. Farsang, A. K. Kleppe, N. P. M. Casati, S. G. MacLeod, S. A. T. Redfern, F.-X. Coudert and T. D. Bennett, *J. Am. Chem. Soc.*, 2019, **141**, 9330–9337.
6 T. D. Bennett and A. K. Cheetham, *Acc. Chem. Res.*, 2014, **47**, 1555–1562.
7 M. Stepniewska, K. Januchta, C. Zhou, A. Qiao, M. M. Smedskjaer and Y. Yue, *Proc. Natl. Acad. Sci. U. S. A.*, 2020, **117**, 10149–10154.
8 R. Gaillac, P. Pullumbi, K. A. Beyer, K. W. Chapman, D. A. Keen, T. D. Bennett and F.-X. Coudert, *Nat. Mater.*, 2017, **16**, 1149–1154.
9 S. Park and H.-K. Jeong, *J. Mater. Chem. A*, 2022, **10**, 4992–4998.
10 A. M. Bumstead, M. L. Ríos Gómez, M. F. Thorne, A. F. Sapnik, L. Longley, J. M. Tuffnell, D. S. Keeble, D. A. Keen and T. D. Bennett, *CrystEngComm*, 2020, **22**, 3627–3637.
11 R. Gaillac, P. Pullumbi and F. X. Coudert, *J. Phys. Chem. C*, 2018, **122**, 6730–6736.
12 E. F. Baxter, T. D. Bennett, A. B. Cairns, N. J. Brownbill, A. L. Goodwin, D. A. Keen, P. A. Chater, F. Blanc and A. K. Cheetham, *Dalton Trans.*, 2016, **45**, 4258–4268.
13 T. D. Bennett, P. J. Saines, D. A. Keen, J. C. Tan and A. K. Cheetham, *Chem. – Eur. J.*, 2013, **19**, 7049–7055.
14 T. D. Bennett, S. Cao, J. C. Tan, D. A. Keen, E. G. Bithell, P. J. Beldon, T. Friscic and A. K. Cheetham, *J. Am. Chem. Soc.*, 2011, **133**, 14546–14549.
15 T. D. Bennett, Y. Yue, P. Li, A. Qiao, H. Tao, N. G. Greaves, T. Richards, G. I. Lampronti, S. A. T. Redfern, F. Blanc, O. K. Farha, J. T. Hupp, A. K. Cheetham and D. A. Keen, *J. Am. Chem. Soc.*, 2016, **138**, 3484–3492.
16 L. Frentzel-Beyme, M. Kloß, P. Kolodzeiski, R. Pallach and S. Henke, *J. Am. Chem. Soc.*, 2019, **141**, 12362–12371.
17 Y. Pan, Y. Liu, G. Zeng, L. Zhao and Z. Lai, *Chem. Commun.*, 2011, **47**, 2071–2073.
18 D. Fairen-Jimenez, S. A. Moggach, M. T. Wharmby, P. A. Wright, S. Parsons and T. Düren, *J. Am. Chem. Soc.*, 2011, **133**, 8900–8902.
19 H. H. M. Yeung, A. F. Sapnik, F. Massingberd-Mundy, M. W. Gaultois, Y. Wu, D. A. X. Fraser, S. Henke, R. Pallach, N. Heidenreich, O. V. Magdysyuk, N. T. Vo and A. L. Goodwin, *Angew. Chem., Int. Ed.*, 2019, **58**, 566–571.
20 C. Mottillo and T. Friščić, *Angew. Chem.*, 2014, **126**, 7601–7604.
21 S. Cao, T. D. Bennett, D. A. Keen, A. L. Goodwin and A. K. Cheetham, *Chem. Commun.*, 2012, **48**, 7805–7807.
22 A. D. Katsenis, A. Puškarić, V. Štrukil, C. Mottillo, P. A. Julien, K. Užarević, M. H. Pham, T. O. Do, S. A. J. Kimber, P. Lazić, O. Magdysyuk, R. E. Dinnebier, I. Halasz and T. Friščić, *Nat. Commun.*, 2015, **6**, 1–8.
23 A. M. Bumstead, M. F. Thorne and T. D. Bennett, *Faraday Discuss.*, 2021, **225**, 210–225.
24 K. S. Park, Z. Ni, A. P. Cote, J. Y. Choi, R. Huang, F. J. Uribe-Romo, H. K. Chae, M. O'Keeffe and O. M. Yaghi, *Proc. Natl. Acad. Sci. U. S. A.*, 2006, **103**, 10186–10191.
25 F. Gándara, F. J. Uribe-Romo, D. K. Britt, H. Furukawa, L. Lei, R. Cheng, X. Duan, M. O'Keeffe and O. M. Yaghi, *Chem. – Eur. J.*, 2012, **18**, 10595–10601.
26 Z. Akimbekov, A. D. Katsenis, G. P. Nagabhushana, G. Ayoub, M. Arhangelskis, A. J. Morris, T. Friščić and A. Navrotsky, *J. Am. Chem. Soc.*, 2017, **139**, 7952–7957.
27 J. López-Cabrelles, E. Miguel-Casañ, M. Esteve-Rochina, E. Andres-Garcia, I. J. Vitórica-Yrezábal, J. Calbo and G. Mínguez Espallargas, *Chem. Sci.*, 2022, **13**, 842–847.
28 T. Kaneshige, H. Sakamoto and M. Ohtani, *Chem. Commun.*, 2022, **58**, 4588–4591.
29 I. Halasz, S. A. J. Kimber, P. J. Beldon, A. M. Belenguer, F. Adams, V. Honkimäki, R. C. Nightingale, R. E. Dinnebier and T. Friščić, *Nat. Protoc.*, 2013, **8**, 1718–1729.
30 A. L. Spek, A. J. M. Duisenberg and M. C. Feiters, *Acta Crystallogr., Sect. C: Cryst. Struct. Commun.*, 1983, **39**, 1212–1214.
31 A. S. Al-Wasidi, I. I. S. AlZahrani, A. M. Naglah, M. G. El-Desouky, M. A. Khalil, A. A. El-Bindary and M. A. El-Bindary, *ChemistrySelect*, 2021, **6**, 11431–11447.

